Nuclear Inst. and Methods in Physics Research B 436 (2018) 285–291

Contents lists available at ScienceDirect

Nuclear Inst. and Methods in Physics Research B

journal homepage: www.elsevier.com/locate/nimb

Latest Geant4 developments for PIXE applications

S. Bakr[a,*], D.D. Cohen[b], R. Siegele[b], S. Incerti[c,d], V. Ivanchenko[e,f], A. Mantero[g], A. Rosenfeld[a,h], S. Guatelli[a,h]

[a] CMRP, University of Wollongong, Australia
[b] Centre for Accelerator Science, Australian Nuclear Science and Technology Organization, Australia
[c] CNRS/IN2P3, Centre d'Etudes Nucléaires de Bordeaux-Gradignan, France
[d] Université de Bordeaux, Centre d'Etudes Nucléaires de Bordeaux-Gradignan, France
[e] Geant4 Associates International Ltd, United Kingdom
[f] Tomsk State University, Russia
[g] SWHARD s.r.l, Italy
[h] Illawarra Health and Medical Research Institute, University of Wollongong, NSW, Australia

ARTICLE INFO

Keywords:
Geant4
PIXE
Ionisation cross sections
ECPSSR

ABSTRACT

We describe the recent inclusion in Geant4 of state-of-the-art proton and alpha particle shell ionisation cross sections based on the ECPSSR approach as calculated by Cohen et al., called here *ANSTO ECPSSR*. The new ionisation cross sections have been integrated into Geant4. We present a comparison of the fluorescence X-ray spectra generated by the *ANSTO ECPSSR* set of cross sections and, alternatively, the currently available sets of Geant4 PIXE cross sections. The comparisons are performed for a large set of sample materials spanning a broad range of atomic numbers. The two alternative PIXE cross sections approaches (Geant4 and ANSTO) have been compared to existing experimental measurements performed at ANSTO with gold, tantalum and cerium targets of interest for nanomedicine applications. The results show that, while the alternative approaches produce equivalent results for vacancies generated in the K and L shell, differences are evident in the case of M shell vacancies. This work represents the next step in the effort to improve the Geant4 modelling of the atomic relaxation and provide recommended approaches to the Geant4 user community. This new Geant4 development is of interest for applications spanning from life and space to environmental science.

1. Introduction

Particle Induced X-ray Emission (PIXE) describes the physical phenomenon of charged particles, such as protons, alpha particles and heavier ions, incident on a target, which ionises some atoms by removing one or more inner shell electrons from the K, L or M shells. The shell vacancy is subsequently filled by an electron of an outer shell. This process is accompanied by the emission of characteristic X-rays or Auger electrons and Coster-Kronig transitions with energies corresponding to the difference in the binding energies of the involved atomic shells.

The Geant4 Toolkit [1] includes analytical and data driven PIXE cross sections for electrons, protons and heavier charged particles [2]. This paper describes the recent inclusion in Geant4 of PIXE cross section for proton and alpha particles, which are based on the state of the art recommendations documented in (Cohen, 2015) [3] (1985, 86 and 89) [4–6], as alternative to the already available other Geant4 PIXE cross sections.

The novel *Geant4 ANSTO ECPSSR* approach provides the ionisation cross section of the K, L and M shells for incident protons and alpha particles in the energy ranges displayed in Table 1.

The advantage of the proposed cross sections is that they have been extensively validated against PIXE experimental measurements by many PIXE labs including the Australian Nuclear Science and Technology Organisation [3]. This project is motivated by the constant effort to improve the physics models of Geant4 by including available state of the art physics models.

This work benefits applications of Geant4 in environmental physics, geology, archaeology, space science and medical physics. It may also impact significantly novel application domains such as nanomedicine, where an accurate modelling of atomic relaxation is required [7]. Schlathölter et al. [8], comments that the underlying nanoscale mechanism of nanoparticle enhancement in proton therapy remains poorly understood and therefore, it is important to accurately characterise the secondary radiation field produced by the protons when incident on high-Z nanoparticles,

* Corresponding author.
E-mail address: sb759@uowmail.edu.au (S. Bakr).

https://doi.org/10.1016/j.nimb.2018.10.004
Received 29 September 2017; Received in revised form 9 September 2018; Accepted 5 October 2018
Available online 17 October 2018
0168-583X/

Table 1
Projectile kinetic energy and target element ranges of the ANSTO ECPSSR cross sections for incident protons and alpha particles.

	Kinetic energy	Target elements		
	K, L, M	K	L	M
Proton	0.2–5.2 MeV	6–92	25–92	60–92
Alpha particle	0.2–20.2 MeV			

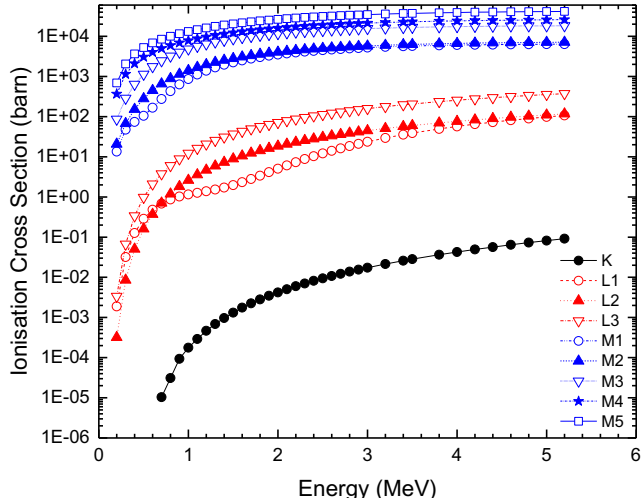

Fig. 1. ANSTO proton ionisation cross sections for K, L and M subshells for a gold target.

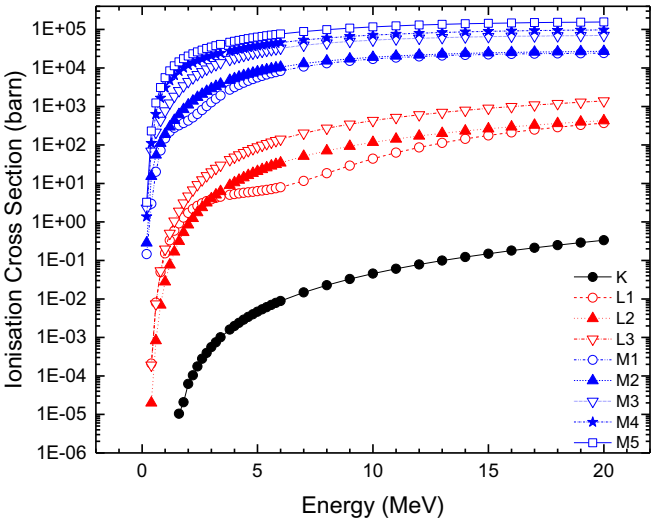

Fig. 2. ANSTO alpha ionisation cross sections for K, L and M subshells for a gold target.

including the characteristics X-rays and Auger electrons deriving from the atomic relaxation. Porcel E et al. [9,10] have shown enhanced damage to DNA in the presence of Pt and Gd nanoparticles irradiated by fast helium ions and carbon ions and comment that Auger electrons play a significant role in the production of indirect damage of the radiation in the biological medium, which needs to be quantified.

2. The Geant4 atomic relaxation

The Geant4 Atomic Relaxation approach includes models for the generation of vacancies in atomic shells and the subsequent emission of

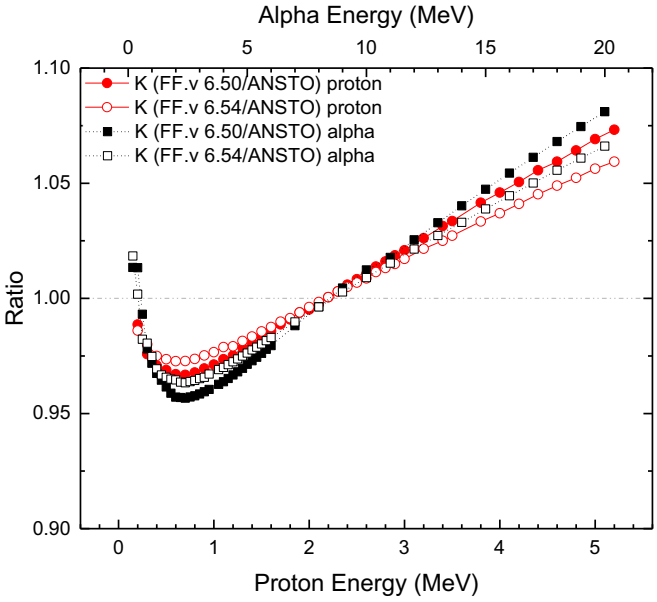

Fig. 3. K shell ionisation cross section ratios for protons and alpha particles incident on a silicon target.

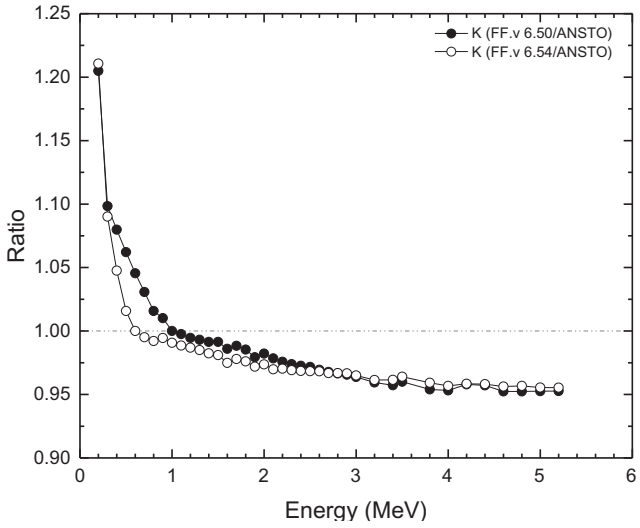

Fig. 4a. K shell ionisation cross section ratios for protons incident on a molybdenum target.

fluorescence X-rays and Auger electrons. The development of this model was firstly described in (Guatelli et al, 2007a) [7], and was then improved in the following years [11,12]. In Geant4, the atomic relaxation simulation is articulated through two stages:

1) The creation of a vacancy by a primary process e.g. photoelectric effect, Compton scattering or ionisation. The shell (or subshell) where the vacancy is created by a process is sampled on the basis of the cross section of the given process. For the ionisation process an additional PIXE cross section is used. At each simulation step of the charged projectile, the vacancies, together with their associated position in space and shell, are sampled according to the PIXE cross section.
2) The relaxation cascade is triggered, starting from the vacancy created by the primary process. Fluorescence X-ray, Auger electrons or Coster-Kronig transitions are generated through radiative and non-radiative transitions, based on the respective transition probabilities and the produced secondary electrons or X-rays are further tracked by Geant4.

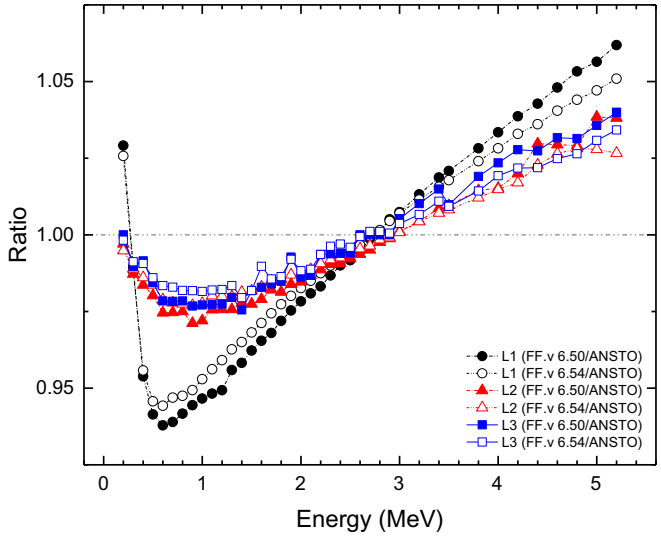

Fig. 4b. L subshells ionisation cross section ratios for protons incident on a molybdenum target.

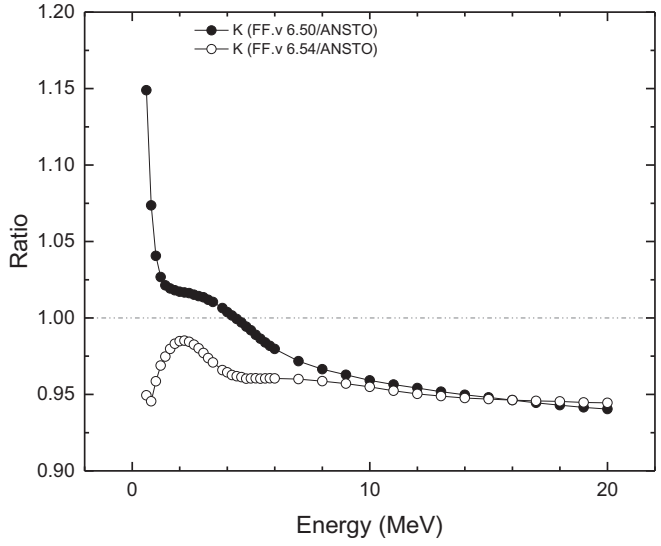

Fig. 5a. K shell ionisation cross section ratios for alpha particles incident on a molybdenum target.

There are currently three alternative PIXE cross sections data sets in Geant4 to generate a vacancy in a shell:

1) The "*Empirical*" set, where K and L shell ionisation cross sections are based on empirical and semi-empirical compilations by Paul et al. and Orlic et al. [13].
2) The "*ECPSSR Form Factor*" set, based on a polynomial approximation of the ionisation cross sections of K, L and a selection of M shells calculated by Taborda et al. using Basbas method but with the ECPSSR theory for incident protons and alpha particles [13].
3) The "*Analytical*" set, based on the ECPSSR theory adapted by Abdelouahed et al. [14], for the description of K and L shells ionisation for incident protons and alpha particles [13].

In addition, it has been possible in Geant4 to simulate any ion, other than proton or alpha, by applying speed and charge scaling to the proton Plane Wave Born Approximation (PWBA) ionisation cross section data sets. However, this approximation is not accurate for slow heavy ions where the Coulomb correction terms, ignored by the PWBA, can become very significant [5,15].

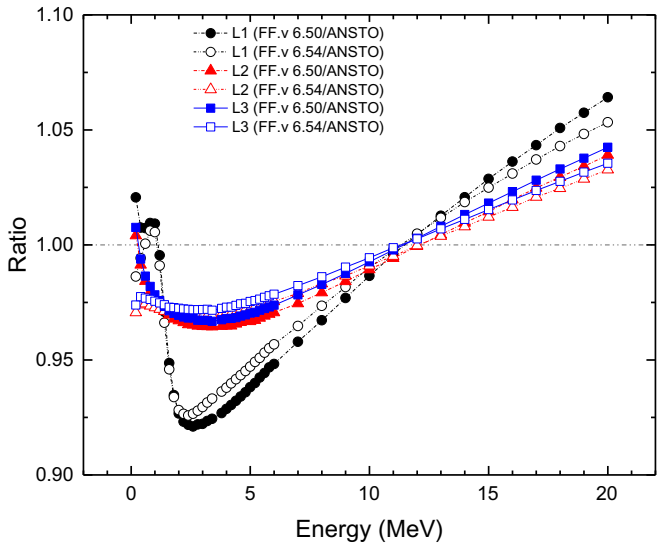

Fig. 5b. L subshells ionisation cross section ratios for alpha particles incident on a molybdenum target.

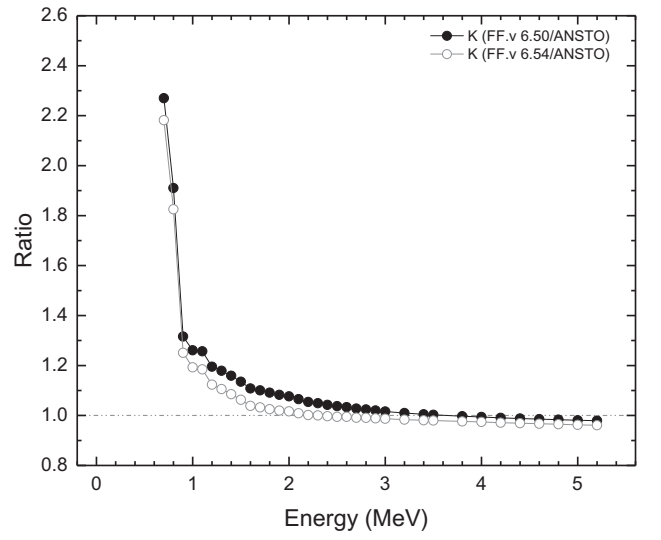

Fig. 6a. K shell ionisation cross section ratios for protons incident on a gold target.

3. Methods

The ECPSSR theory has been developed by Brandt and Lapicki for both K and L subshell ionisation by light ions (Z_1/Z_2) < 0.3, where Z_1 and Z_2 refer to the charges of the projectile and the target atom, respectively [15]. Cohen and Harrigan published ECPSSR K and L subshell ionisation cross sections for both protons and alpha particles bombardment for ion energies from 0.2 to 10 MeV and for a wide variety of target atoms, from carbon to curium. These tables supersede all previous tables of this type as they supply actual ionisation cross sections and do not rely on the scaling of some universal cross section function to obtain the required cross sections [3–6].

Once included in the Geant4 toolkit, the *ANSTO ECPSSR* cross sections have been compared directly to the alternative data sets already available in Geant4 to assess the level of agreement of the different approaches. The impact of the alternative ionisation cross section sets, *ANSTO ECPSSR* and *ECPSSR Form Factor,* has been quantified in terms of number of fluorescence X-rays generated per incident projectile. 13 target materials (Al, Si, Fe, Zr, Te, Ce, Gd, Dy, Ta, W, Pt, Au,

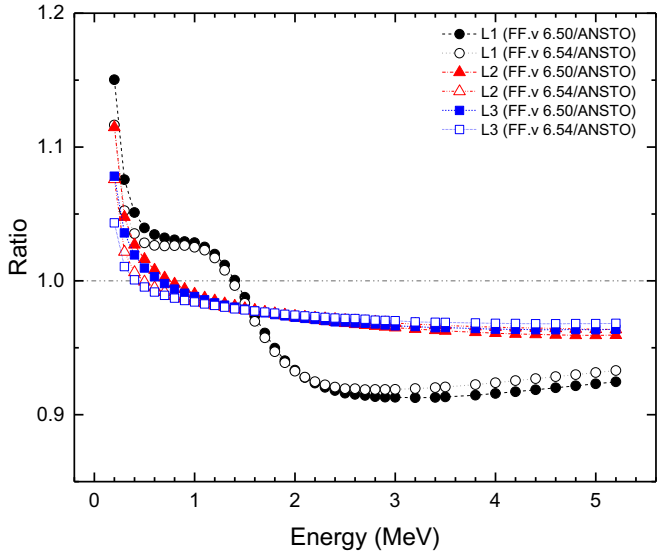

Fig. 6b. L subshells ionisation cross section ratios for protons incident on a gold target.

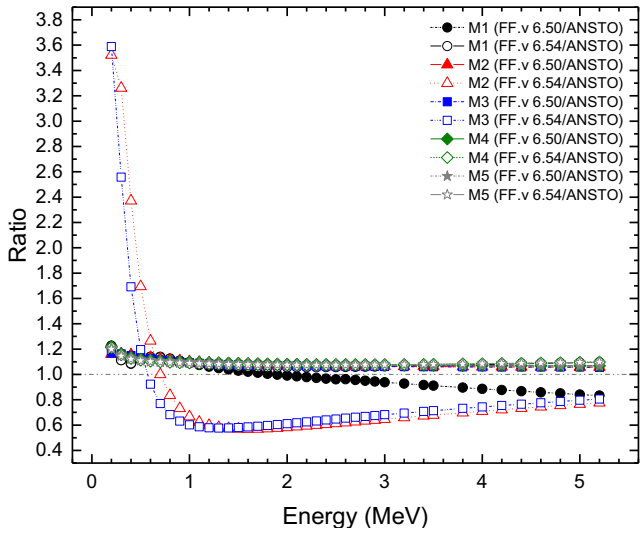

Fig. 6c. M subshells ionisation cross section ratios for protons incident on a gold target.

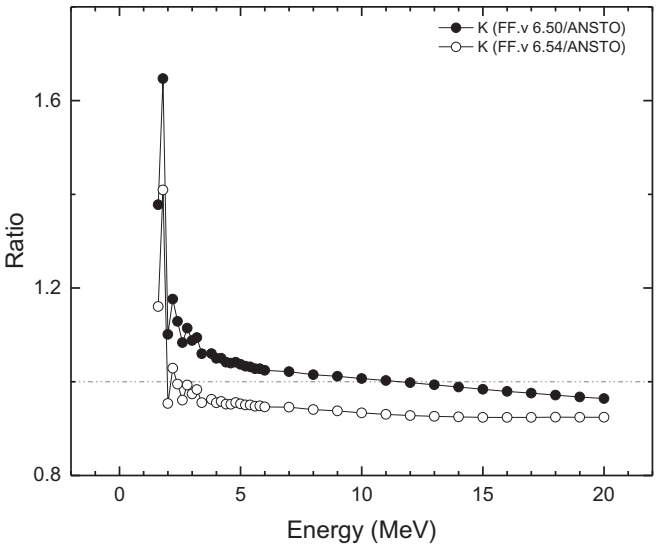

Fig. 7a. K shell ionisation cross section ratios for alpha particles incident on a gold target.

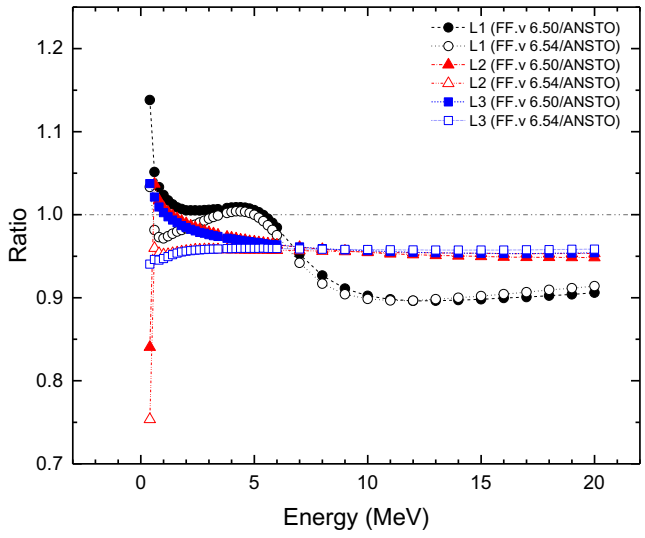

Fig. 7b. L subshells ionisation cross section ratios for alpha particles incident on a gold target.

U) have been chosen, from low to high atomic number Z.

Monochromatic beams of protons (1, 2.5, 3, 5 MeV) and alpha particles (5, 9.5, 15 MeV) are incident on 25 μm thick targets along the direction of the incident beam. The lateral sizes are 50 μm. The production threshold of secondary particles is ignored. The fluorescence X-rays have been counted once they are generated in the target. The default atomic relaxation library of Geant4, based on the Evaluated Atomic Data Library EADL [16], has been used to calculate the emission rates of the fluorescence X-ray, once the vacancy has been generated [13]. Two different versions of the *ECPSSR Form Factor* have been considered in this work, which are included in *G4EMLOW 6.50* and *G4EMLOW 6.54* data libraries. The *G4EMLOW 6.50* and *G4EMLOW 6.54* are the Low Energy Electromagnetic data libraries, released with Geant4 10.3 and Geant4 10.4 beta versions, respectively. Note that the existing Geant4 PIXE *Empirical* and *Analytical* cross section sets [11] have not been considered in this work as they generate only K and L vacancies.

Finally, the Geant4 PIXE Package, with the *ANSTO ECPSSR* cross sections, has been compared to experimental measurements performed at ANSTO using the 6 MV SIRIUS Tandem Accelerator. In this case, protons and alpha particles are incident on 25 nm thick cerium and tantalum and 100 nm thick gold targets along the direction of the incident beam, similarly to the ANSTO experimental set-up. Using a 3 MeV proton beam, cerium, tantalum and gold targets are considered because of their possible application in High-Z nanoparticle radio-enhancement in proton therapy [17,18]. In addition, a tantalum target has been used for 10 MeV alpha particle beam. Relative fluorescence spectra are presented.

3.1. Experimental setup

PIXE spectra were experimentally measured at the ANSTO heavy ion microprobe beamline using 3 MeV proton and 10 MeV He^{2+} ion beams with currents varying between 0.5 and 2.5 nA. For X-ray detection, a 100 mm^2 high purity Ge detector with a solid angle of 90 msr was used. The detector has a 25 μm thick Be window. To prevent the scattered protons from entering the detector and to reduce the low energy X-ray yield from light elements such as the underlying Si in some of the samples, a 100 μm thick Mylar absorber (or filter) was

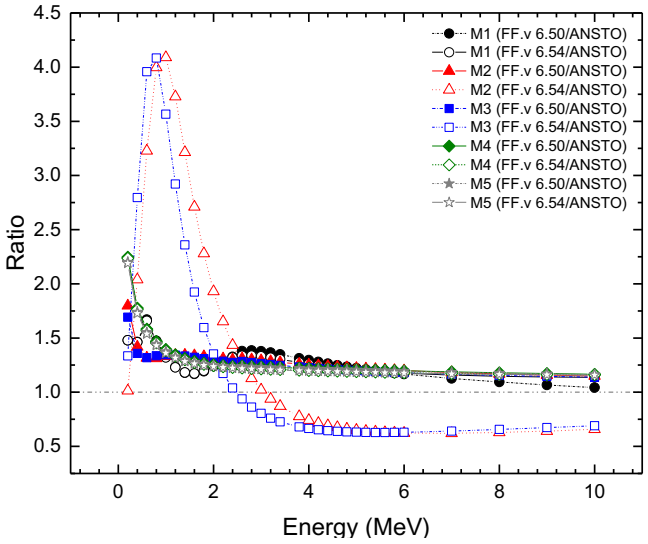

Fig. 7c. M subshells ionisation cross section ratios for alpha particles incident on a gold target.

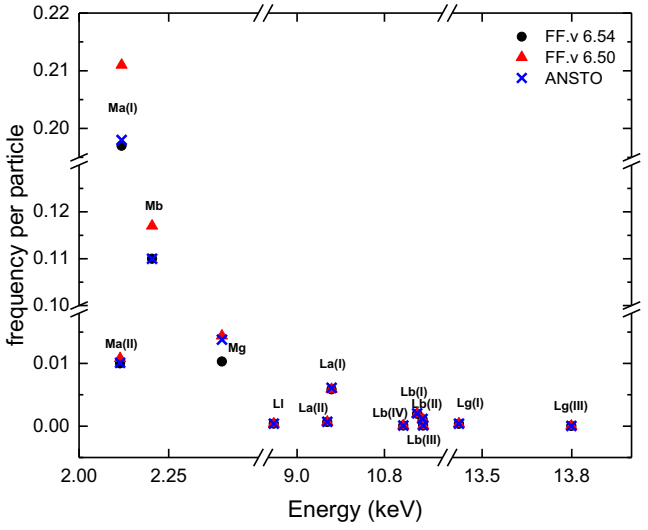

Fig. 8. X-ray emission generated by 3 MeV incident protons incident on a gold target.

placed in front of the detector. The data were collected using the Data Acquisition System mpsys4 from Melbourne University together with a Canberra Model 2060 digital signal processor. The irradiated samples were 100 nm thick Au layer on silicon and 25 nm TaO layer on graphite. Additionally, a sample of CeO_2 embedded in a boron oxide pellet was used.

4. Results

4.1. Ionisation cross section comparison

The proposed ANSTO ionisation cross sections have been calculated for all elements. As example Figs. 1 and 2 show the cross sections for a gold target against the kinetic energy of incident protons and alpha particles, respectively.

As expected, the cross sections increase with the vacancy being originated in the K, L and M shells/subshells.

The ionisation cross sections calculated by means of the *ECPSSR Form Factor* with both *G4EMLOW 6.50* and *6.54* libraries and *ANSTO*

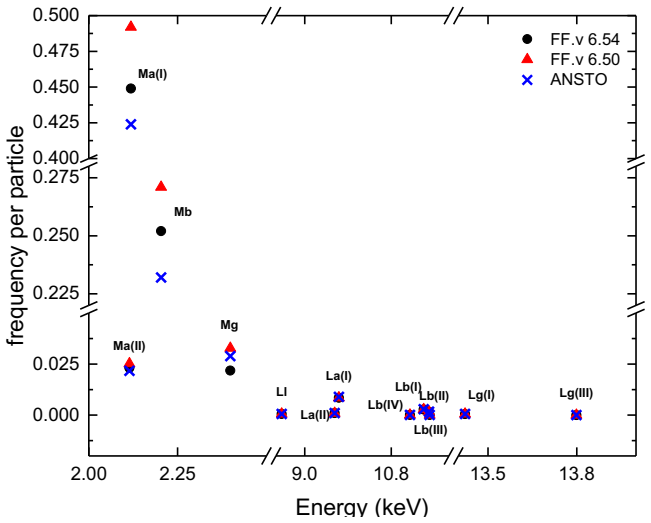

Fig. 9. X-ray emission generated by 9.5 MeV alpha particles incident on a gold target.

Table 2
Number of X-rays generated in the gold target per incident 3 MeV proton, when adopting different cross sections approaches (ANSTO ECPSSR, Form Factor ECPSSR, Analytical and Empirical).

	ANSTO	Form Factor v. 6.50	Form Factor v. 6.54	Analytical	Empirical
Mα(II)	1.01E−02	1.08E−02	1.00E−02	4.36E−05	3.89E−05
Mα(I)	1.98E−01	2.11E−01	1.97E−01	8.19E−04	7.77E−04
Mβ	1.10E−01	1.17E−01	1.10E−01	4.17E−04	4.09E−04
Mγ	1.38E−02	1.44E−02	1.03E−02	5.47E−05	5.48E−05
Ll	3.97E−04	3.84E−04	3.91E−04	4.03E−04	3.85E−04
Lα(II)	6.95E−04	6.72E−04	6.61E−04	7.00E−04	6.69E−04
Lα(I)	6.12E−03	5.89E−03	5.88E−03	6.17E−03	5.84E−03
Lβ(IV)	9.78E−05	9.30E−05	8.82E−05	1.02E−04	8.50E−05
Lβ(I)	2.03E−03	1.95E−03	1.98E−03	2.04E−03	2.17E−03
Lβ(II)	1.15E−03	1.09E−03	1.11E−03	1.16E−03	1.10E−03
Lβ(III)	1.16E−04	1.01E−04	9.64E−05	1.14E−04	9.73E−05
Lγ(I)	4.03E−04	3.92E−04	3.84E−04	4.01E−04	4.30E−04
Lγ(III)	3.00E−05	2.99E−05	3.02E−05	3.04E−05	2.62E−05
Kα(I)	1.38E−06	1.08E−02	2.00E−06	4.36E−05	3.89E−05

Table 3
Number of X-rays generated in the gold target per incident 9.5 MeV alpha particle, when adopting different cross sections approaches (ANSTO ECPSSR, Form Factor ECPSSR, Analytical and Empirical).

	ANSTO	Form Factor 6.50	Form Factor 6.54	Analytical	Empirical
Mα(II)	2.17E−02	2.52E−02	2.31E−02	5.83E−05	6.17E−05
Mα(I)	4.24E−01	4.92E−01	4.49E−01	1.16E−03	1.16E−03
Mβ	2.32E−01	2.71E−01	2.52E−01	5.83E−04	5.85E−04
Mγ	2.89E−02	3.28E−02	2.18E−02	7.90E−05	8.01E−05
Ll	5.84E−04	5.54E−04	5.57E−04	5.77E−04	5.75E−04
Lα(II)	1.02E−03	9.62E−04	9.75E−04	1.01E−03	1.01E−03
Lα(I)	8.93E−03	8.52E−03	8.48E−03	8.87E−03	8.88E−03
Lβ(IV)	9.37E−05	8.46E−05	8.58E−05	9.54E−05	9.54E−05
Lβ(I)	2.87E−03	2.75E−03	2.78E−03	2.84E−03	2.86E−03
Lβ(II)	1.66E−03	1.59E−03	1.59E−03	1.66E−03	1.66E−03
Lβ(III)	1.06E−04	9.79E−05	9.96E−05	1.07E−04	1.09E−04
Lγ(I)	5.72E−04	5.44E−04	5.38E−04	5.57E−04	5.63E−04
Lγ(III)	2.77E−05	2.78E−05	2.66E−05	2.98E−05	2.97E−05

ECPSSR approaches were compared for a set of different target materials. In this work, *G4EMLOW 6.50* and *6.54* ionisation cross sections libraries are called *ECPSSR Form Factor v. 6.50* and *v. 6.54,* respectively.

Figs. 3–7 show the ratio $R = \frac{\sigma_{ECPSSR\_Form\_Factor}}{\sigma_{ECPSSR\_ANSTO}}$, for K, L and M shells

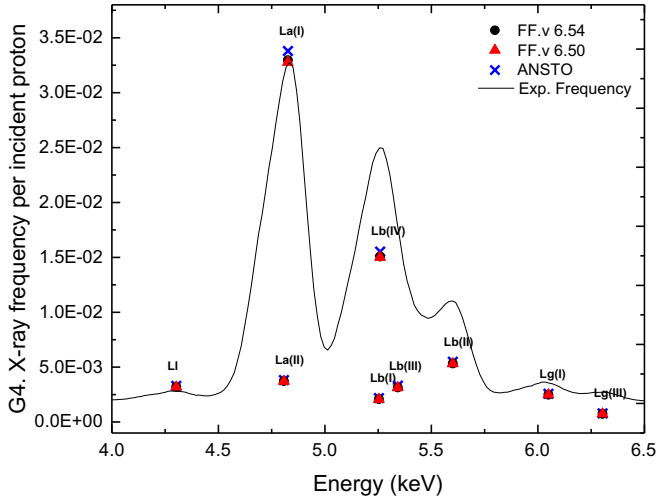

Fig. 10. Geant4 Cerium X-ray emissions generated by a 3 MeV incident proton compared to the experimental spectrum.

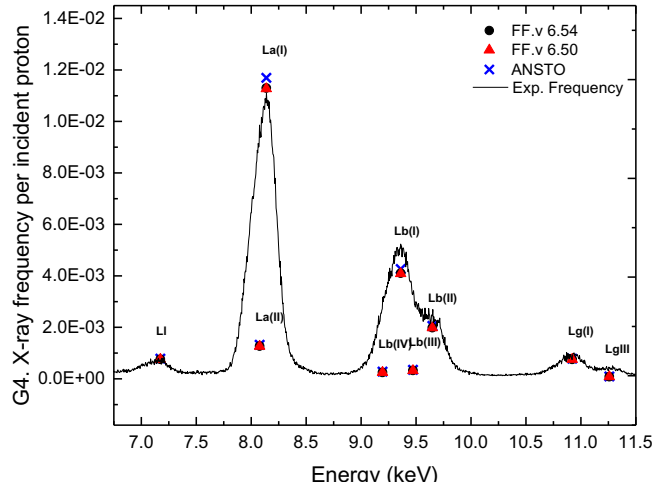

Fig. 11. Geant4 tantalum X-ray emissions generated by a 3 MeV incident proton compared to the experimental spectrum.

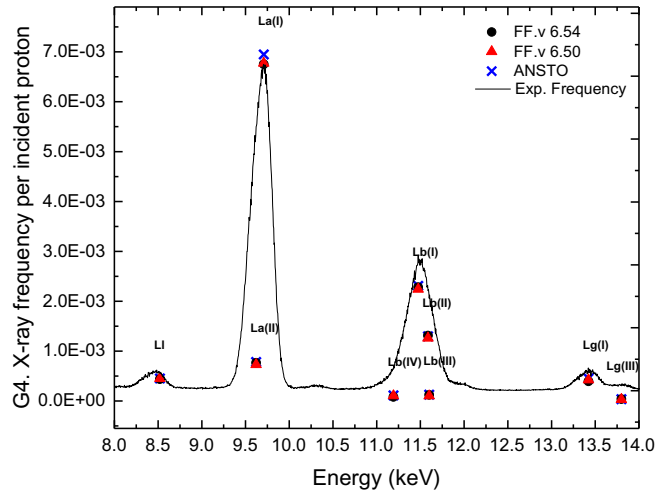

Fig. 12. Geant4 gold X-ray emissions generated by a 3 MeV incident proton compared to the experimental spectrum.

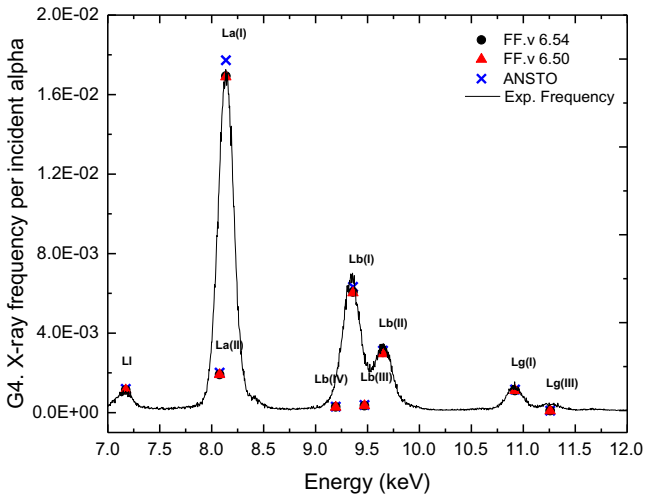

Fig. 13. Geant4 tantalum X-ray emissions generated by a 10 MeV incident alpha compared to the experimental spectrum.

and subshells with respect to the incident proton and alpha particle kinetic energy for low (silicon), medium (molybdenum) and high Z (gold) target materials. These figures illustrate how ANSTO's calculated ionisation cross sections behave in comparison to Geant4 *ECPSSR Form Factor* ones.

It can be observed that in general, for the K shell, an agreement within ± 10% was observed for proton energies below 2.5 MeV for low Z target materials. Larger differences (~25%) are observed for high Z targets materials for proton energies below 1.5 MeV. Differences up to ~10% are observed for incident alpha particles of kinetic energies higher than 15 MeV for low Z sample materials, while differences within ~10% are observed for high Z sample materials for all considered incident alpha particle energies higher than 4 MeV.

For L subshells, the differences are less than ± 5% for all proton energies lower than 3 MeV, while they are less than 20% in the range 3–5.2 MeV for medium Z targets. For high Z materials differences, up to ~10% are observed in the entire proton kinetic energy range. Differences between 10% and 20% are observed for medium and high Z targets, respectively, for the entire alpha particle energy range.

The K and L subshells ionisation cross sections of the *ECPSSR Form Factor model* are closer to the *ANSTO ECPSSR* when calculated by means of the Geant4 Low Energy EM library 6.54 version.

For M subshells, the differences between *ECPSSR Form Factor-v. 6.50* and *ANSTO ECPSSR* are less than 20% for all proton energies less than 1 MeV, while they are less than 10% in the range 1–5.2 MeV, except for the M1 subshell ionisation cross sections. In this case the differences are up to 40% for the entire proton energy range. Differences up to ~25% and ~15% have been found for alpha particles with energy 0.2 – 3 MeV and 3 – 10 MeV, respectively. In contrast, for M2 and M3 subshells, there are significant differences (~300%) for *ECPSSR Form Factor v. 6.54* data sets when compared to *ECPSSR Form Factor v. 6.50* and *ANSTO ECPSSR*.

In general, it can be observed that differences are within ~25% for *ECPSSR Form Factor v. 6.50* and *ANSTO ECPSSR*. At lower energies, for both incident protons and alpha particles, the *ECPSSR Form Factor* predicts consistently higher cross sections for all K, L and M subshells. At higher energies and Z sample materials it seems that this trend inverts with the *ANSTO ECPSSR* producing more ionisations for M1 and L subshells.

4.2. Modelling X-ray emission by means of the ANSTO ECPSSR cross sections

As an example of X-ray emission generated with the *ANSTO ECPSSR* cross sections, Figs. 8 and 9 show the X-ray emission calculated in gold,

deriving from vacancies in the L and M subshells generated by an incident 3 MeV proton and 9.5 MeV alpha particles, respectively. The results are compared for the *ECPSSR Form Factor v. 6.50*, *v. 6.54* and *ANSTO ECPSSR* data sets. The standard deviation of these results is less than 1.5%. No X-ray lines are shown for the Geant4 *Analytical* and *Empirical* approaches because they do not provide ionisation cross sections for the M subshells. It can be observed that the X-ray emission rates generated with the *ECPSSR Form Factor* in the case of M subshells are higher than the ones generated with the *ANSTO ECPSSR* cross sections. This reflects the fact that the *ECPSSR Form Factor* cross section is higher than the *ANSTO ECPSSR* one, as shown in Fig. 6c. The emission rates of X-rays deriving from vacancies in the L subshells are almost identical (see Figs. 8 and 9).

Tables 2 and 3 list the number of X-rays generated in a gold target per incident 3 MeV proton and 9.5 MeV alpha particle, respectively. For M-lines, it is clear that the frequency calculated via *ECPSSR Form Factor* cross section is higher than the one calculated with the *ANSTO ECPSSR* data set. For L-lines, the closest model to *ANSTO ECPSSR* is the Geant4 *Analytical* model and the probabilities obtained with the *ECPSSR Form Factor* and *Empirical sets* are lower than *ANSTO ECPSSR*.

4.3. Validation of the Geant4 PIXE Package against experimental measurements

The X-ray emissions calculated by the Geant4 PIXE Package with the *ANSTO ECPSSR* and *ECPSSR Form Factor* ionisation cross sections, have been compared against experimental spectra.

Figs. 10–13 show the comparison of the X-ray emission frequencies per incident particle, calculated by means of ANSTO and Form Factor cross sections, against experimental measurements. The Geant4 X-ray emissions have been normalized to the highest peak of the experimental spectra. Results are shown for incident protons and alpha particles for the targets under study. It can be observed that the X-ray emission rates calculated with the *ANSTO ECPSSR* cross sections are slightly higher than those generated using the *ECPSSR Form Factor (v. 6.50, v. 6.54)*, in agreement with Figs. 6c and 7c.

The results show a good agreement between Geant4-calculated emission X-ray spectra and the experimental measurements. The ANSTO and Form Factor ECPSSR cross sections produce very similar results, because of their limited differences in the case of the L subshells. Bigger differences are expected when the vacancy is produced in the M subshells.

5. Conclusions

ANSTO ECPSSR cross sections for protons and alpha particles have been integrated in Geant4 for PIXE simulation. The *ECPSSR Form Factor* and *ANSTO ECPSSR* approaches can handle the M subshell relaxations. The two alternative sets, while providing more comparable results for K and L shells, show significant differences when modelling the M shell, which may have a significant impact in Geant4-based nanomedicine studies. For the future, it is recommended to validate the alternative sets of ionisation cross sections for this shell with accurate, reference experimental measurements, when available [19].

The novel cross sections, called ANSTO ECPSSR, will be included in the public release of Geant4 and can be selected in a Geant4 user application by means of user interface commands on top of any electromagnetic physics configurations.

Acknowledgments

This project has been funded by the Australian Research Council, grant number ARC DP 170100967. The authors D. D. Cohen and R. Siegele would like to acknowledge National Collaborative Research Infrastructure Strategies (NCRIS) for funding of the Centre for Accelerator Science (CAS) and to CAS staff for access to their ion beam analysis facilities.

References

[1] S. Agostinelli, J. Allison, K. Amako, et al., Geant4—a simulation toolkit, Nucl Instrum. Methods Phys. Res. Sect. A Accel. Spectrom., Det. Assoc. Equip. 506 (3) (2003) 250–303, https://doi.org/10.1016/S0168-9002(03)01368-8.
[2] J. Allison, K. Amako, J. Apostolakis, et al., Recent developments in Geant4, Nucl. Instrum. Methods Phys. Res. Sect. A Accel. Spectrom., Det. Assoc. Equip. 835 (2016) 186–225.
[3] D.D. Cohen, J. Crawford, R. Siegele, K, L, and M shell datasets for PIXE spectrum fitting and analysis, Nucl. Instrum. Methods Phys. Res. Sect. B Beam Interact Mater. Atoms. 363 (2015) 7–18, https://doi.org/10.1016/j.nimb.2015.08.012.
[4] D.D. Cohen, M. Harrigan, K- and L-shell ionization cross sections for protons and helium ions calculated in the ecpssr theory, At. Data Nucl. Data Tables 33 (2) (1985) 255–343, https://doi.org/10.1016/0092-640X(85)90004-X.
[5] D.D. Cohen, M. Harrigan, L shell line intensities for light ion induced X-ray emission, Nucl Instrum. Methods Phys. Res. Sect. B Beam Interact Mater Atoms. 15 (1) (1986) 576–580, https://doi.org/10.1016/0168-583X(86)90367-8.
[6] D.D. Cohen, K- and L-shell ionization cross sections for deuterons calculated in the ECPSSR theory, At. Data Nucl. Data Tables 41 (2) (1989) 287–338, https://doi.org/10.1016/0092-640X(89)90021-1.
[7] S. Guatelli, A. Mantero, B. Mascialino, P. Nieminen, M.G. Pia, Geant4 Atomic Relaxation, IEEE Trans. Nucl. Sci. 54 (3) (2007) 585–593, https://doi.org/10.1109/tns.2007.896214.
[8] T. Schlathölter, P. Eustache, E. Porcel, et al., Improving proton therapy by metal-containing nanoparticles: nanoscale insights, Int J Nanomed. 11 (2016) 1549 https://www.dovepress.com/getfile.php?fileID=29896.
[9] E. Porcel, O. Tillement, F. Lux, et al., Gadolinium-based nanoparticles to improve the hadrontherapy performances, Nanomedicine 10 (8) (2014) 1601–1608, https://doi.org/10.1016/j.nano.2014.05.005.
[10] E. Porcel, S. Li, N. Usami, et al., Nano-Sensitization under gamma rays and fast ion radiation, Journal of Physics: Conference Series, IOP Publishing, 2012, p. 12006.
[11] A. Mantero, Abdelouahed H Ben, C. Champion, et al., PIXE simulation in Geant4, X-Ray Spectrom. 40 (3) (2011) 135–140.
[12] S. Incerti, B. Suerfu, J. Xu, Simulation of Auger electron emission from nanometer-size gold targets using the Geant4 Monte Carlo simulation toolkit, Nucl. Instrum. Methods Phys. Res. Sect. B Beam Interact Mater Atoms. 372 (Supplement C) (2016) 91–101, https://doi.org/10.1016/j.nimb.2016.02.005.
[13] S. Incerti, P. Barberet, G. Deves, et al., Comparison of experimental proton-induced fluorescence spectra for a selection of thin high-Z samples with Geant4 Monte Carlo simulations, Nucl Instrum. Methods Phys. Res. Sect B Beam Interact Mater Atoms. 358 (2015) 210–222.
[14] Abdelouahed H. Ben, S. Incerti, A. Mantero, New Geant4 cross section models for PIXE simulation, Nucl Instrum. Methods Phys. Res. Sect. B Beam Interact Mater. Atoms 267 (1) (2009) 37–44.
[15] W. Brandt, G. Lapicki, Energy-loss effect in inner-shell Coulomb ionization by heavy charged particles, Phys. Rev. A 23 (4) (1981) 1717–1729, https://doi.org/10.1103/PhysRevA.23.1717.
[16] S.T. Perkins, D.E. Cullen, M.H. Chen, J. Rathkopf, J. Scofield, J.H. Hubbell, Tables and Graphs of Atomic Subshell and Relaxation Data Derived from the LLNL Evaluated Atomic Data Library, ${Z} = 1-100$. Eadl. 1991;30:UCRL-50400. doi:10.2172/10121422.
[17] S. McKinnon, S. Guatelli, S. Incerti, et al., Local dose enhancement of proton therapy by ceramic oxide nanoparticles investigated with Geant4 simulations, Phys. Med. Eur. J. Med. Phys. 32 (12) (2016) 1584–1593.
[18] E. Engels, S. Corde, S. McKinnon, et al., Optimizing dose enhancement with Ta 2 O 5 nanoparticles for synchrotron microbeam activated radiation therapy, Phys. Med. 32 (12) (2016) 1852–1861.
[19] D.D. Cohen, E. Stelcer, J. Crawford, A. Atanacio, G. Doherty, G. Lapicki, Comparison of proton and helium induced M subshell X-ray production cross sections with the ECUSAR theory, Nucl. Instrum. Methods Phys. Res. Sect. B Beam Interact Mater. Atoms 318 (2014) 11–14.